Designing Structurally Ordered Pt/Sn Nanoparticles in Ionic Liquids and their Enhanced Catalytic Performance

Christine Dietrich,[a, b] Martin Hähsler,[a, b] Wu Wang,[c, f] Christian Kübel,[c, d, e] and Silke Behrens*[a, b]

Abstract: Multimetallic nanoparticles (NPs) often exhibit enhanced catalytic properties that differ from their parent materials. Carefully exploring the structures of multimetallic NPs is a prerequisite for understanding the structure- and composition-associated properties. Herein, intermetallic Pt/Sn NPs with tunable compositions are designed exploiting the beneficial properties of ionic liquids (ILs) in a one-pot synthetic procedure. Metal salt precursors are reduced with triethylhydridoborate, whereby the cation of the triethylhydridoborate is adapted to the cation of the IL. Both the initial metal precursor ratio and the type of IL influence the structure of the NPs, with the effect of the IL being more pronounced. PtSn nanocrystals are obtained as phase pure products under optimized reaction conditions, whereby a microwave-assisted approach leads to higher crystallinity. In the hydrogenation of α,β-unsaturated aldehydes, the catalytic performance obviously depend on the NP composition. In bimetallic Pt/Sn NPs, higher Pt content leads to increased conversion, while increase in Sn increases selectivity to the cinnamic alcohol.

Introduction

Transition metal nanoparticles (NPs) are among the most relevant catalysts in the field of catalysis.[1] Due to the large industrial production scales, even small improvements in catalytic performance or a reduction in (precious) metal content

[a] Dr. C. Dietrich, Dr. M. Hähsler, PD Dr. S. Behrens
     Institute of Catalysis Research and Technology
     Karlsruhe Institute of Technology (KIT)
     Hermann-von-Helmholtz-Platz 1, 76344 Eggenstein-Leopoldshafen (Germany)
     E-mail: silke.behrens@kit.edu
[b] Dr. C. Dietrich, Dr. M. Hähsler, PD Dr. S. Behrens
     Institute of Inorganic Chemistry
     Ruprechts-Karls University Heidelberg
     Im Neuenheimer Feld 270, 69120 Heidelberg (Germany)
[c] Dr. W. Wang, Prof. Dr. C. Kübel
     Institute of Nanotechnology
     Karlsruhe Institute of Technology (KIT)
     Hermann-von-Helmholtz-Platz 1, 76344 Eggenstein-Leopoldshafen (Germany)
[d] Prof. Dr. C. Kübel
     Karlsruhe Nano Micro Facility (KNMF)
     Karlsruhe Institute of Technology (KIT)
     Hermann-von-Helmholtz-Platz 1, 76344 Eggenstein-Leopoldshafen (Germany)
[e] Prof. Dr. C. Kübel
     Department of Earth & Geosciences
     Technical University Darmstadt
     Alarich-Weiss-Str. 2, 64287 Darmstadt (Germany)
[f] Dr. W. Wang
     Department of Physics
     Southern University of Science and Technology, Shenzhen, Guangdong, 518055 (P. R. China)

can have significant economic and environmental impacts. In this context, multimetallic NPs have attracted considerable interest due to multiple functionalities and prominent catalytic activity and selectivity as well as thermal and chemical stability over their monometallic counterparts.[2] Enhanced catalytic properties were attributed to synergistic effects, such as ensemble effects where different surface atoms take distinct mechanistic functionalities, geometric effects where the spatial arrangement of surface atoms is influenced by structure, strain and size and/or electronic effects where the d-band center position is shifted to lower or higher energies. Due to enhanced catalytic activity and selectivity, bimetallic Pt/Sn NPs, for example, are used as heterogeneous catalysts in various types of reactions, including oxidation,[3] reduction,[4] and hydrogenation reactions.[5] Selective hydrogenation of α,β-unsaturated aldehydes to unsaturated alcohols is an essential step in the production of fine chemicals[6] and the conversion of biomass-derived compounds.[7] Although thermodynamics favors formation of saturated aldehydes over that of unsaturated alcohols, the latter can be selectively produced on bimetallic Pt-based catalysts by tailoring size, composition, facets and support material. Electron transfer was achieved by incorporation of electropositive metals (e.g. Sn, Ge, or Fe),[8] whereby the electron-deficient metal atoms acted as Lewis acid adsorption sites for C=O. This shows that the selectivity of Pt-based bimetallic NPs is determined by a complex set of factors that needs to be considered and addressed in their synthesis.

A variety of methods has been used to prepare Pt/Sn-based NPs and supported catalysts using conventional solvents and stabilizers.[9] Recently, a one-pot synthesis of Pt/Sn NPs *via* chemical reduction of the metal salts with borohydrides was described.[2c,10] Catalytic performance and NP stability not only depend on the overall NP composition and architecture (e.g. core-shell, Janus-type, or alloyed NPs) but also on the atomic ordering (e.g. substitutional solid-solution alloys *vs.* ordered

intermetallic compounds) which may lead to enhanced thermal and chemical stability and catalytic behavior.[2a,b,11] For example, formation enthalpies ΔH_f of PtSn and Pt$_3$Sn are −74.0 and −55.3 kg mol^{-1}, respectively, suggesting high stability of these intermetallic compounds.[2a] The disorder-to-order transition where the randomly mixed alloy equlibrates into an ordered intermetallic phase, however, typically requires high temperatures and thus, the synthesis of ordered intermetallic NPs is challenging.[2b] Synthesis of intermetallic Pt$_3$Sn, PtSn and PtSn$_2$ NPs was achieved by co-reduction of the precursors and subsequent annealing in a KCl or LiCl matrix or by polyol reduction in octadecene.[9] Alternatively, Pt$_3$Sn- and PtSn-based NPs were obtained *via* a *ship-in-the-bottle* synthesis from Pt NPs stabilized in a mesoporous SiO$_2$ shell at high temperatures.[5c,12] Room-temperature ILs reveal unique physico-chemical properties (i.e., excellent solvent properties, low vapor pressure, high polarity, and wide electrochemical stability window) which have been exploited for the synthesis of various types of NPs.[13] NP nucleation and growth processes in ILs are controlled by weakly coordinating anions and cations, which also act as (electro)steric stabilizers against NP agglomeration.[13–14] The IL not only influences the synthesis and catalytic properties of the metal NPs[15] but can itself act as a selectivity promoter during catalysis.[16] While the synthesis of bimetallic NPs has been described in ILs, relatively little is known about the ordering behavior and formation of intermetallic NPs in ILs as well as their catalytic performance.[17]

Here, we explore various types of ILs for the synthesis of intermetallic Pt/Sn-based NPs and study their ordering behavior. The catalytic performance of the intermetallic NP catalysts is investigated in the selective hydrogenation of cinnamaldehyde.

Results and Discussion

Nanoparticle synthesis in ILs

In ILs, weakly coordinating IL anions and cations control both particle nucleation and growth processes.[2c,14a,18] Semi-organized clusters of IL anions and cations provide protective layers which stabilize the as-formed NPs. Intermetallic Pt/Sn-based NPs were prepared in ILs by one-step co-reduction of the two metal precursors (i.e., PtCl$_2$ and Sn(ac)$_2$ or SnCl$_2$). Appropriate choice of the anion, the cation and its alkyl side chain can regulate size and distribution of Sn in the particles.[18–19] In this study, ILs combining different IL cations and anions were used as a reaction medium, i.e. methyltrioctylammonium bis(trifluoromethylsulfonyl)imide [OMA][NTf$_2$], 1-butyl-3-methyl-imidazolium bis(trifluoromethyl-sulfonyl)imide [BMIm][NTf$_2$], 1-butyl-3-methylimidazolium tetrafluoroborate [BMIm][BF$_4$], and 1-butyl-3-methylimidazolium hexafluorophosphate [BMIm][PF$_6$]. Methyltrioctylammonium triethylhydridoborate [OMA][BEt$_3$H] was employed as a reducing agent for NP synthesis in [OMA][NTf$_2$], while [BMIm][BEt$_3$H] was used as a reducing agent for synthesis in [BMIm][NTf$_2$], [BMIm][BF$_4$], and [BMIm][PF$_6$]. Potassium or lithium triethylhydridoborate (i.e., superhydride) have been previously applied as strong reducing agents for NP

synthesis. In this case, alkali halogenides (e.g., KCl, KBr, or LiCl) are formed as by-products which are typically precipitated and separated from the NP sol, e.g. by subsequent cooling. In general, these alkali halide salts are highly soluble in ILs, and it is very difficult to remove these by-products from the NP sol after synthesis. Bönnemann *et al.* have initially reported on the combination of tetraalkylammonium stabilizers (*e.g.* N(octyl)$_4^+$) with [BEt$_3$H]$^-$ which they used for the synthesis of various transition metal colloids.[20] Here, we coupled the respective IL cations (i.e., [OMA]$^+$ or [BMIm]$^+$) by salt metathesis with the reducing agent to form [OMA][BEt$_3$H] or [BMIm][BEt$_3$H], accordingly, thereby avoiding contamination of the IL-stabilized nanoparticles with alkali metal ions. No additional ligands or surfactants were employed for NP synthesis in the IL. In a typical synthesis, the reducing agent (*i.e*, [OMA][BEt$_3$H] or [BMIm][BEt$_3$H]) was rapidly injected into the solution of the metal salts in the IL at 60 °C. Then the reaction mixture was heated at 200 °C for several hours. NP formation was indicated by H$_2$ evolution and a color change from light brown to brown-black. NP sols of high colloidal stability were obtained in the ILs. NP sols in [OMA][NTf$_2$], for example, were stable for several months. In this study, the influence of the metal salt precursors (*i.e.*, PtCl$_2$ and Sn(ac)$_2$ or SnCl$_2$), their molar ratio and the IL anion and cation on the composition and structure of the bimetallic Pt/Sn-based NPs was investigated.

The PtSn bulk phase diagram contains five compounds (Pt$_3$Sn, PtSn, Pt$_2$Sn$_3$, PtSn$_2$, PtSn$_4$) with narrow phase widths.[9c] In particular, the Pt-rich phases Pt$_3$Sn and PtSn seem to be attractive catalysts for many types of reaction.[5c,21] With respect to this, an initial molar Pt:Sn precursor ratio of 3:1 was set as a starting point for NP synthesis. Recently, Pt/Sn-based nanoparticles of 2–3 nm diameter with random-type alloyed structure were prepared in [OMA][NTf$_2$] at low reaction temperature.[2c] In order to prepare NPs with intermetallic composition and structure, the reduction temperature was initially kept at 60 °C, but followed by a successive annealing step at 200 °C.

The reduction of PtCl$_2$ and Sn(ac)$_2$ (molar Pt:Sn precursor ratio of 3:1) in [OMA][NTf$_2$] yielded NPs **1** (Figure 1). XRD analysis of NPs **1** (Figure 1a) revealed the characteristic reflections at 39°, 45°, 66°, 79°, 114° and 119° (2θ), corresponding to the (111), (200), (220), (311), (331) and (420) planes of the face-centered cubic (fcc) Pt$_3$Sn phase (see Figure S3 for the indexed XRD pattern). Since the scattering power of Sn and Pt is similar and the Sn content is low, superlattice peaks for Pt$_3$Sn are typically weak and were not detected. Shoulders occurring at slightly higher Bragg angles of the Pt$_3$Sn reflections indicated the presence of Pt (i.e., 40°, 45°, 68°, and 82° (2θ)) and SnO$_2$ (i.e., reflections at 26°, 33° and 52° (2θ)) which was formed by decomposition of Sn(ac)$_2$.[2c] Phase composition as determined by Rietveld analysis revealed mainly Pt (48%) in addition to Pt$_3$Sn (16%) and SnO$_2$ (35%). High resolution transmission electron microscopy (HRTEM) images are in agreement with the formation of Pt$_3$Sn and/or Pt NPs as well as of some SnO$_2$ particles with an average particle diameter of 8.5 nm (Figure 1b).
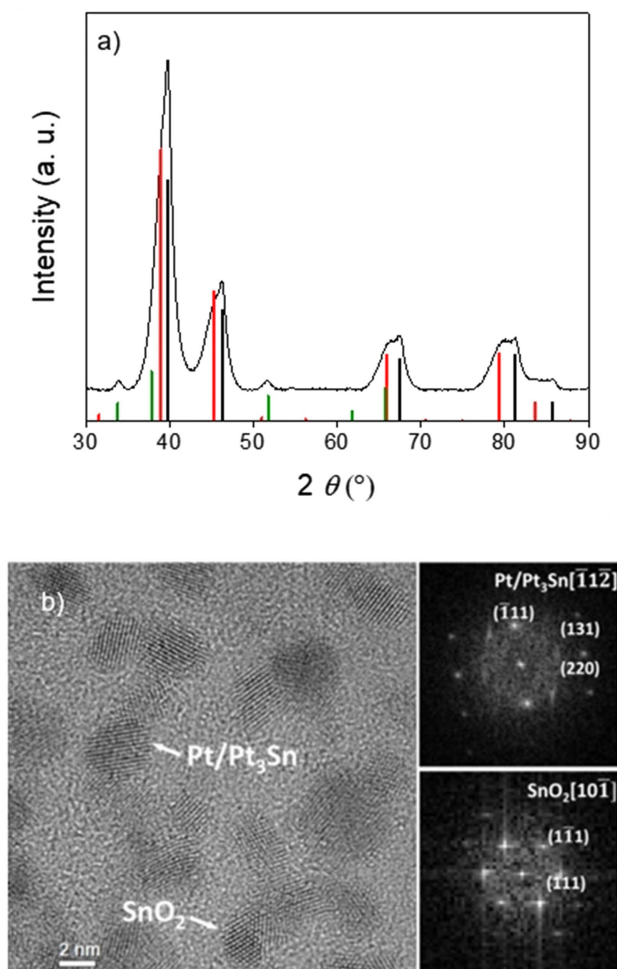
Figure 1. NPs **1** synthesized in [OMA][NTf$_2$] using a molar PtCl$_2$:Sn(ac)$_2$ ratio of 3:1: a) X-ray diffraction pattern indicating the formation of Pt (black), SnO$_2$ (green) and the intermetallic Pt$_3$Sn phase (red). b) HRTEM image with indexed fast Fourier transform patterns of the marked NPs.

To prevent SnO$_2$ formation, SnCl$_2$ was used instead of Sn(ac)$_2$ in the following experiments under otherwise same reaction conditions. Additionally, in order to tune the phase composition of the NPs, the molar PtCl$_2$/SnCl$_2$ ratio was increased from 3:1 over 3:2 to 3:3, resulting in NPs **2**, **3**, and **4** (Scheme 1, Table 1). The size, elemental composition and the structure of the NPs were analyzed by transmission electron microscopy (TEM, HRTEM, scanning transmission electron microscopy with high angle annular detector (STEM-HAADF)) with
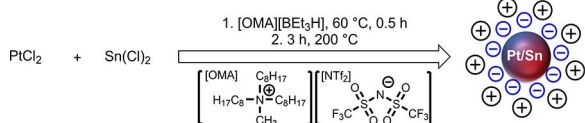
Scheme 1. Illustration of reaction conditions employed in the synthesis of NPs **2**, **3** and **4** in [OMA][NTf$_2$]: To prevent SnO$_2$ formation, SnCl$_2$ was used instead of Sn(ac)$_2$. In order to tune the phase composition of the NPs, the influence of the molar PtCl$_2$/SnCl$_2$ ratio was investigated and increased from 3:1 over 3:2 to 3:3.

energy-dispersive X-ray spectroscopy (EDS) and XRD analysis (Table 1). The crystallite size of NPs was calculated using the Scherrer equation. It should be noted that Rietveld analysis is typically employed for highly crystalline samples (crystallite sizes 100 nm) and for small NPs with sizes below 10 nm the error of the fit increases.

In the case of NPs **2**, where the Pt:Sn ratio was 3:1 but SnCl$_2$ was employed instead of Sn(ac)$_2$, the diffraction pattern (Figure 2a) revealed mainly intermetallic Pt$_3$Sn NPs (50%). Characteristic reflections of the hexagonal PtSn phase at 25°, 30°, 41°, 44°, 51°, 54°, 56°, 62°, 72° 75°, 79°, 81° and 85° (2θ) and superlattice peaks in the 50–60° and 65–75° (2θ) region also indicated the formation of ordered, intermetallic PtSn NPs (30%) (see Figure S4 for the indexed XRD pattern). In addition, some Pt NPs (20%) were observed (shoulders at 68° and 82° (2θ)). HRTEM images showed individual NPs consisting either of intermetallic PtSn (Figure 2c) or Pt$_3$Sn (Figure 2d). Pt$_3$Sn and Pt NPs could not be distinguished on the basis of HRTEM, but the STEM-EDX map indicates bimetallic particles, as the Pt and Sn distribution seem to mostly match each other (Figure 2a).

When the amount of SnCl$_2$ precursor was increased (molar Pt/Sn ratio 3:2), no monometallic Pt phase was observed and NPs **3** were formed. Here, the formation of the hexagonal PtSn phase (68%) was preferred instead of Pt$_3$Sn (see Figure S5 for the indexed XRD pattern). TEM images revealed NPs of irregular shape with an average size of 5.6 nm (Figure 2b) which was in good agreement with the PtSn crystallite size of 5.2 nm based
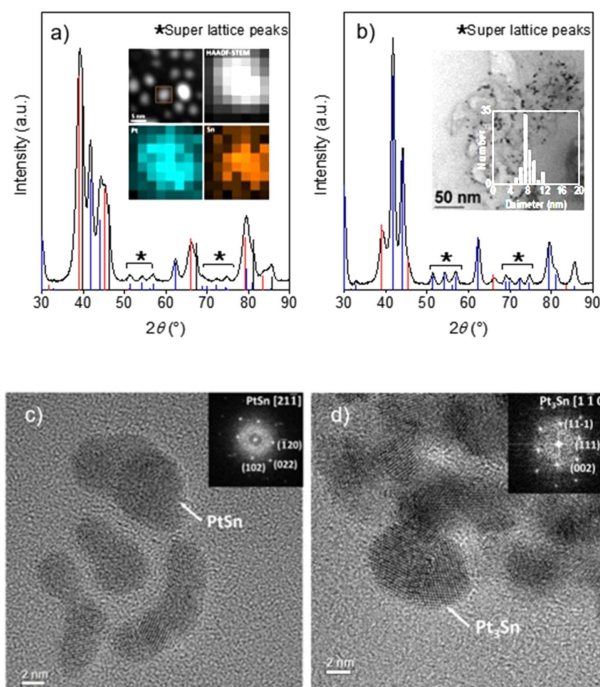

Figure 2. XRD analysis of a) NPs **2** with HAADF-STEM image and corresponding elemental maps obtained (in the area marked with box) indicating the formation of intermetallic Pt$_3$Sn-phase (red), PtSn-phase (blue) and Pt (black). b) XRD analysis of NPs **3** with TEM image and size histogram indicating the formation of intermetallic Pt$_3$Sn-phase (red), PtSn-phase (blue). HRTEM images of c) PtSn and d) Pt$_3$Sn in NPs **2** with indexed fast Fourier transforms of the marked NPs.

Table 1. Size and composition of NPs obtained by reduction of PtCl$_2$/SnCl$_2$ in [OMA][NTf$_2$] (reduction at 60 °C; annealing at 200 °C for 3 h).

NPs	Molar Pt:Sn ratio	Particle size d in [nm] TEM	XRD (hkl)[a]	Composition[b] [%]
2	3:1	8.1	PtSn: 11.8 (101) Pt$_3$Sn: 5.6 (331) Pt: 3.9 (111)	Pt$_3$Sn (50%) PtSn (30%) Pt (20%)
3	3:2	5.6	PtSn: 5.2 (101) Pt$_3$Sn: 3.5 (200)	Pt$_3$Sn (32%) PtSn (68%)
4	3:3	n.a.	PtSn: 4.7 (102) Pt: 2.3 (111)	PtSn (32%) Pt (68%)

[a] Particle size calculated according to Scherrer equation for reflections given in brackets; [b] Phase composition according to Rietveld analysis (references: SnO$_2$ (ICCD 98–001-6635), Sn (ICCD 98–005-3790), Pt (ICCD 98–007-6153), PtSn (ICCD 98–065-8326); Pt$_3$Sn (ICDD 98–018-3076)).
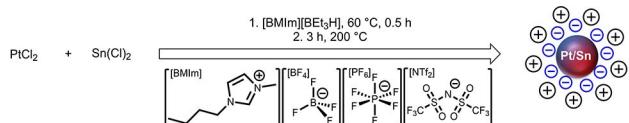
on Scherrer equation. Further increase in the amount of SnCl$_2$ precursor, however, did not result in the formation of a phase pure NP product. Surprisingly, when the amount of SnCl$_2$ precursor was further increased in NPs **4** (molar Pt/Sn ratio 1:1), XRD analysis revealed monometallic Pt (68%) as main product and less PtSn (32%) (see Figure S2 for the indexed XRD pattern). This clearly showed that the control of the phase composition based on the molar precursor ratio alone (see supporting information) was limited.

We have previously demonstrated the strong influence of the chemical nature of the IL on the formation and stability of Co NPs. In this case, the NPs were synthesized by thermal decomposition of Co$_2$(CO)$_8$ in a series of ILs. Due to the large (electro)steric repulsion radius of the [OMA]$^+$ cation, Co NP sols were most stable in [OMA][NTf$_2$].[2c,19] Although the Pt/Sn NP-based sols in [OMA][NTf$_2$] also showed high colloidal stability, no phase pure NP product could be received by reducing PtCl$_2$ and SnCl$_2$ in [OMA][NTf$_2$], regardless of the precursor ratio.

Scheme 2. Illustration of reaction conditions employed in the synthesis of NPs **6**, **7** and **8a** in different ILs: Imidazolium-based ILs (i.e., [BMIm][PF$_6$] (NPs **6**), [BMIm][NTf$_2$] (NPs **7**), [BMIm][BF$_4$] (NPs **8a,b**)) were chosen to investigate the influence of IL cation and anion on the formation of Pt/Sn NPs. For NPs **8b**, microwave irradiation was employed to heat the reaction mixture.

Therefore, we chose three commonly used imidazolium-based ILs (i.e., [BMIm][PF$_6$], [BMIm][BF$_4$] and [BMIm][NTf$_2$]) to investigate the influence of IL cation and anion on the formation of Pt/Sn NPs (Scheme 2).

The molar Pt:Sn precursor ratio was maintained at 3:1. Size and composition of the resulting NPs are given in Table 2. In [BMIm][PF$_6$] amorphous NPs **6** were obtained, while the same synthetic procedure in [BMIm][NTf$_2$] resulted in the formation of intermetallic PtSn NPs (69%) in addition to some monometallic Pt NPs (31%) in NPs **7**.

However, well-ordered and phase-pure, intermetallic PtSn NPs **8** were obtained as a single-phase product in [BMIm][BF$_4$]. The diffraction pattern of NPs **8a** (Figure 3a) showed the characteristic reflections of the ordered hexagonal PtSn phase (JCPD 03–065-0959) at 25°, 30°, 33°, 41°, 44°, 51°, 54°, 56°, 57°, 62°, 68°, 70°, 72°, 74°, 79°, 81°, 85°, 97°, 102°, 105°, 107°, 112° and 119° (2θ) (see Figure S6 for the indexed XRD pattern). No peaks remained unaccounted, excluding the formation of any other Pt-, Sn- or Pt/Sn-based phase. The presence of super lattice peaks (denoted with brackets in Figure 3a in the 50–60° and 65–75° (2θ) region) further confirm that the NPs adopted the ordered hexagonal PtSn structure. According to Scherrer equation, the size of the PtSn NPs **8a** was 12.2 nm which was larger than the mean diameter of 2.9 ($\pm$0.7) nm of the particles based on TEM analysis (Figure 3b). It might be possible that the discrepancy of NP sizes based on XRD and TEM analysis here is an artefact of TEM grid preparation. One has to keep in mind that for determination of NP sizes different aspects regarding

Table 2. Size and composition of Pt/Sn-based NPs obtained by reduction of PtCl$_2$ and SnCl$_2$ in different ILs (molar Pt:Sn precursor ratio 3:1; reduction at 60 °C; annealing at 200 °C for 3 h).

NPs	IL	Particle size d [nm] TEM	XRD (hkl)[a]	Composition[%][b]
6	[BMIm][PF$_6$]	n.a.	–	amorphous
7	[BMIm][NTf$_2$]	n.a.	PtSn: 10.6 (102)	PtSn (69) Pt (31)
8a	[BMIm][BF$_4$]	2.9[d]	PtSn: 12.2 (202)[d]	PtSn
8b[c]	[BMIm][BF$_4$]	2.4[d]	PtSn: 10.9 (102)[d]	PtSn

[a] Particle size calculated according to Scherrer equation for reflections given in brackets; [b] Phase composition according to Rietveld analysis (references used for Rietveld analysis: SnO$_2$ (ICCD 98-001-6635), Sn (ICCD 98-005-3790), Pt (ICCD 98–007-6153), PtSn (ICCD 98-065-8326); Pt$_3$Sn (ICDD 98-018-3076); [c] Microwave irradiation (settings: 1) 60 °C, 10 W for 30 min; 2) 10 W, 200 °C for 1 h). [d] It should be noted that the annealing time for NPs **8a** (conventional heating) was also slightly longer (2 h, 200 °C) than in case of microwave heating (NPs **8b**). Both increased annealing time and microwave heating during NP nucleation may have affected the size of the NPs.
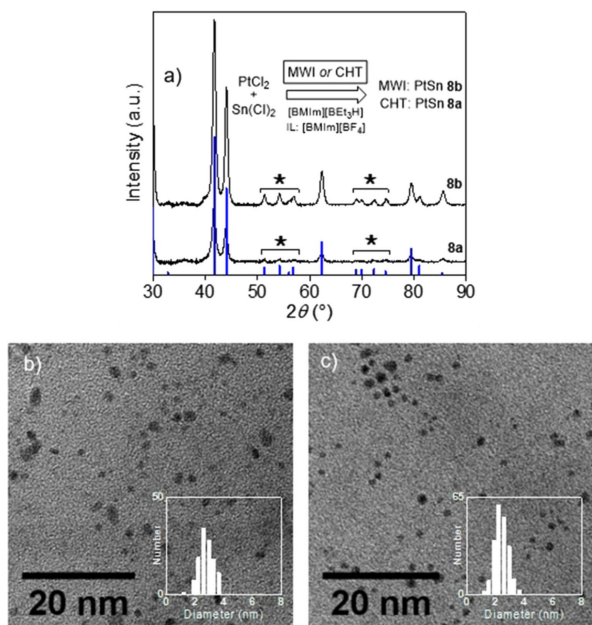
Figure 3. Comparison of XRD patterns: Phase pure PtSn NPs (blue) **8a** and **8b** obtained *via* conventional and microwave heating, respectively. The super lattice peaks are marked with (⋆). TEM images with corresponding size distributions of b) PtSn NPs **8a** and c) **8b**.

sampling and statistics may arise.[22] TEM analysis of NPs stabilized in ILs is by no means trivial; the IL is typically removed as much as possible (e.g. by suspending and /or washing steps using volatile, conventional organic solvents) in order to improve image quality and avoid image contamination in the electron beam.[2c,23] In our case, NPs were suspended in THF for preparation of TEM grids which is immiscible with [BMIm][BF$_4$]. It could be that a small fraction of larger NPs was not adequately stabilized during sampling for TEM grid preparation. On the other side, crystal sizes determined by the Scherrer formula are volume-weighted averages and thus, more representative for a larger volume of the sample. However, the Scherrer formula does not consider particle size distributions; if both large and small NPs are present in the sample, the diffraction profile represents a convolution of narrow and broad reflections, whereby the narrow peaks of larger NPs dominate the profile.[24] Apparently, heating the reaction mixture by microwave irradiation stimulated the nucleation of a highly ordered and crystalline PtSn phase in NPs **8b**. While superlattice peaks were quite weak for NPs **8a**, they were clearly pronounced for NPs **8b**. In general, microwave irradiation is rapid way to homogeneously heat reaction mixtures leading to highly reproducible results (Figure 3a).[25] This will be subject of future investigations. The size of PtSn NPs **8b** was 10.9 nm according to Scherrer equation, while TEM images revealed almost spherical PtSn NPs of 2.4 ($\pm$0.5) nm (Figure 3c) However, in our experiments, only [BF$_4$]$^-$ or [PF$_6$]$^-$based ILs (*i.e.*, [BMIm][BF$_4$] or [BMIm][PF$_6$]) were suitable for microwave-assisted NP synthesis while [NTf$_2$]$^-$based ILs (*i.e.*, [OMA][NTf$_2$] and [BMIm]

[NTf$_2$]) were decomposed under microwave irradiation as visually indicated by the formation of a white smoke.

Figure 4 provides an overview of the impact of the molar PtCl$_2$/SnCl$_2$ ratio and the nature of IL on the phase composition by comparing the diffraction pattern of the NPs synthesized under otherwise same reaction conditions. Monometallic Pt NPs **9** were synthesized as a reference using a similar synthetic protocol. The diffraction pattern of the Pt NPs revealed four reflections at 40°, 45°, 68°, and 82° (2θ) which were in good agreement with the fcc Pt phase. The appearance of reflections at 41 and 44° (2θ) and of superlattice peaks in the region 50–60° (2θ) indicated the formation of PtSn.

UV-vis spectroscopy studies

Binary Pt–Sn complexes and zintl clusters have been previously reported to induce compositionally homogeneous nuclei after co-reduction, which resulted in the formation of intermetallic NPs with a well-ordered structure.[9c,26] It is well-known that Pt(II) chlorides and Sn(II) chlorides form a variety of different complexes and clusters in solution.[25–27] Therefore, complex formation of the PtCl$_2$ and SnCl$_2$ precursors in the ILs was investigated for [OMA][NTf$_2$] and [BMIm][BF$_4$] by UV-vis spectroscopy. UV-vis spectra of the individual PtCl$_2$ and SnCl$_2$ precursors were compared to the pre-reduction solutions containing both precursors in different molar ratios in [OMA][NTf$_2$] and [BMIm][BF$_4$] (see SI, Figure S1) (Table S1).

The UV-vis spectra of the PtCl$_2$/SnCl$_2$ mixtures in [OMA][NTf$_2$], showed absorption peaks at 359 nm and 353 nm for a molar Pt:Sn precursor ratio of 3:1 and 3:2, respectively (Figure 5). Compared to the spectra of the individual precursor solutions (PtCl$_2$: 435 nm; SnCl$_2$: 280 nm, 316 nm), the spectra of the mixtures showed new absorption peaks with their maxima depending on the molar Pt:Sn precursor ratio and thus indicating the formation of binary Pt–Sn complexes in the IL prior to reduction. For the solutions of both precursors in
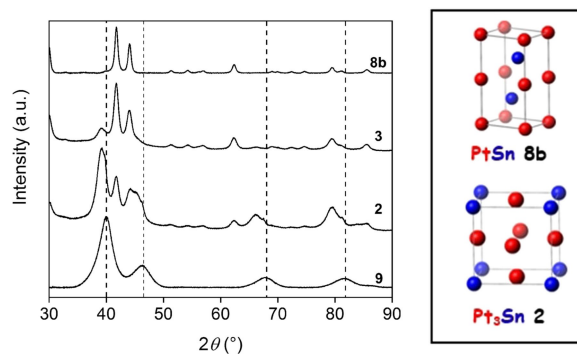

Figure 4. Influence of the molar Pt:Sn ratio and the nature of IL on the NP phase composition: Pt reference NPs **9** (dotted lines: Pt reference); NPs **2** (Pt/Sn precursor ratio 3:1; composition: Pt$_3$Sn (50%), PtSn (30%), Pt (20%)); NPs **3** (Pt/Sn precursor ratio 3:2; composition: Pt$_3$Sn (32%), PtSn (68%)); NPs **8b** (Pt/Sn precursor ratio 3:1; composition: PtSn (100%)). [OMA][NTf$_2$] was used in synthesis of NPs **2**, **3**, and **9**, while [BMIm][BF$_4$] and microwave irradiation were employed for synthesis of NPs **8b**. b) Illustration of the cubic Pt$_3$Sn and the hexagonal PtSn phase.
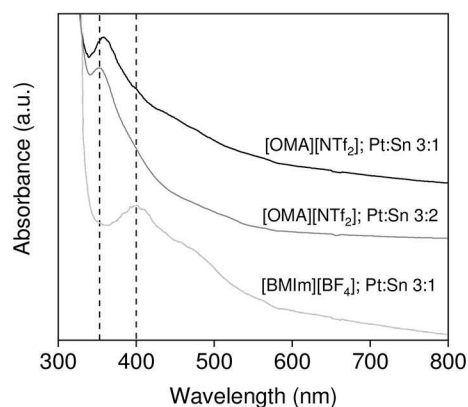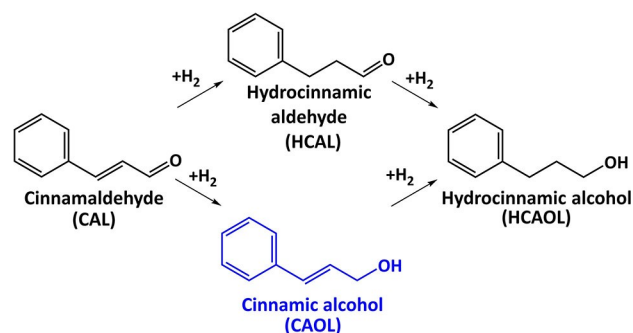
Figure 5. UV-vis spectra of PtCl$_2$/SnCl$_2$ mixtures in [OMA][NTf$_2$] and [BMIm][BF$_4$].

Scheme 3. Reaction pathways and reaction intermediates and products in the hydrogenation of cinnamic aldehyde.

[BMIm][BF$_4$] (molar Pt:Sn ratio 3:1), the peak maximum was clearly shifted to 397 nm, indicating the formation of a different type of binary Pt–Sn complex as compared to the respective solutions in [OMA][NTf$_2$]. Due to the strong impact of the nature of pre-reduction complex on the phase composition of the resulting nanoparticles, PtSn NPs **8a** and **8b** were obtained as a single-phase product in [BMIm][BF$_4$] from PtCl$_2$:SnCl$_2$ (3:1), while the same reaction in [OMA][NTf$_2$] resulted in a mixture of Pt, Pt$_3$Sn, and PtSn.

Catalytic performance

Bimetallic NPs reveal enhanced activities and selectivities which differ from their monometallic counterparts as well as unique properties that exist only in nm-size particles. Small NPs are typically the most active, but due to their high surface energy they tend to aggregate, leading to a reduced catalytic performance. Therefore, for catalytic applications NPs are usually stabilized on a support which facilitates catalyst recycling. The catalytic activity and selectivity of metal NPs dispersed in a liquid medium are often different from those of classical heterogeneous or homogeneous catalysts and therefore, NP sols are often referred to as *quasi-homogeneous* catalysts. Strongly coordinating ligands are usually required not only to synthesize but also to stabilize the NPs in solution. These ligands strongly influence catalytic properties and may poison the NP surface but also boost their catalytic performance. ILs stabilize NPs by interaction with weakly coordinating IL anions

and cations and NP sols of very high colloidal stability are formed.

The selective hydrogenation of cinnamaldehyde (CAL) is a suitable model reaction to probe the influence of the catalyst composition and structure on the selectivity. Three main reaction products (*i.e.*, hydrocinnamic aldehyde (HCAL), cinnamic alcohol (CAOL), and hydrocinnamic alcohol (HCAOL) can be formed *via* the competitive hydrogenation of the C=C bond and/or the carbonyl group (see Scheme 3). The hydrogenation of the C=C bond is thermodynamically favored, and thus, the saturated carbonyls are typically obtained. On monometallic Pt, the reactants preferentially adsorb by π-complexing of the C=C bond, which is successively hydrogenated to yield HCAL. To increase the selectivity to CAOL, the binding energy of the C=C bond should either be lowered (*e.g.*, by radial expansion of the d-bands) or the hydrogenation of the C=O bond should be favored. This can be realized by alloying Pt with electropositive metals such as Sn, Ge or Fe. The performance of our IL-stabilized NPs catalysts in the selective hydrogenation of CAL was investigated in a Teflon-lined autoclave in 10 bar H$_2$ at 80 °C (Pt/Sn NPs@IL (1–3 mL), CAL (17 mmol) in THF (30 mL)). During the reaction, hydrogen was continuously supplied *via* a gas burette; the reaction products were determined by gas chromatography (Table 3). Hydrogenation of CAL in the presence of monometallic Pt NPs yielded the saturated aldehyde (HCAL) as the only reaction product.[2c]

Surprisingly, the phase-pure, intermetallic PtSn NPs stabilized in [BMIm][BF$_4$] (NPs **8a** and **8b**) were catalytically not active. Similar effects have been reported for other metal nanocatalysts stabilized in [BMIm][BF$_4$] suggesting that the NP

Table 3. Monometallic Pt and Pt/Sn-based NPs stabilized in [OMA][NTf$_2$] in the catalytic hydrogenation of CAL (reaction conditions: 10 bar H$_2$, 80 °C). Conversion X_{CAL} and selectivity S were determined by GC after 3 h.

NPs	Phase	n_{metal} [µmol]	X CAL [%]	S CAOL [%]	S HCAOL [%]	S HCAL [%]	Y CAOL [%]
9	Pt	50	5	0	0	100	0
1	Pt, Pt$_3$Sn, SnO$_2$	30	60	52	12	36	31
3	PtSn, Pt$_3$Sn	60	37	88	0	12	32

surface was blocked by fluoride species derived from the $[BF_4]^-$ anion.[28]

The hydrogenation of CAL in the presence of the monometallic Pt reference (NPs **9**) yielded the saturated aldehyde (HCAL) as the only reaction product (Table 3). A significantly higher conversion and selectivity to the α,β-unsaturated cinnamic alcohol (CAOL) was observed for intermetallic NPs **1** (Pt/Pt$_3$Sn/SnO$_2$) and NPs **3** in [OMA][NTf$_2$] (PtSn/Pt$_3$Sn). The time courses of the chemoselective hydrogenation of cinnamaldehyde in presence of NPs **1** and NPs **3** are given in Figure 6. While NPs **1** revealed higher conversion (X_{CAL} 60% after 3 h) than NPs **3** (X_{CAL} 37% after 3 h), the overall CAOL yield was similar for both catalysts (Y_{CAOL} 32% for NPs **1** and 31% for NPs **2** after 3 h of reaction). Nevertheless, no fully hydrogenated product (HCAOL) was formed when the reaction was catalyzed by NPs **3** (PtSn/Pt$_3$Sn), while the NPs **1** also yielded HACOL (Y_{HCAOL} 7%). It has to be noted that NPs **1** also contained some Pt which may have contributed to the observed results.
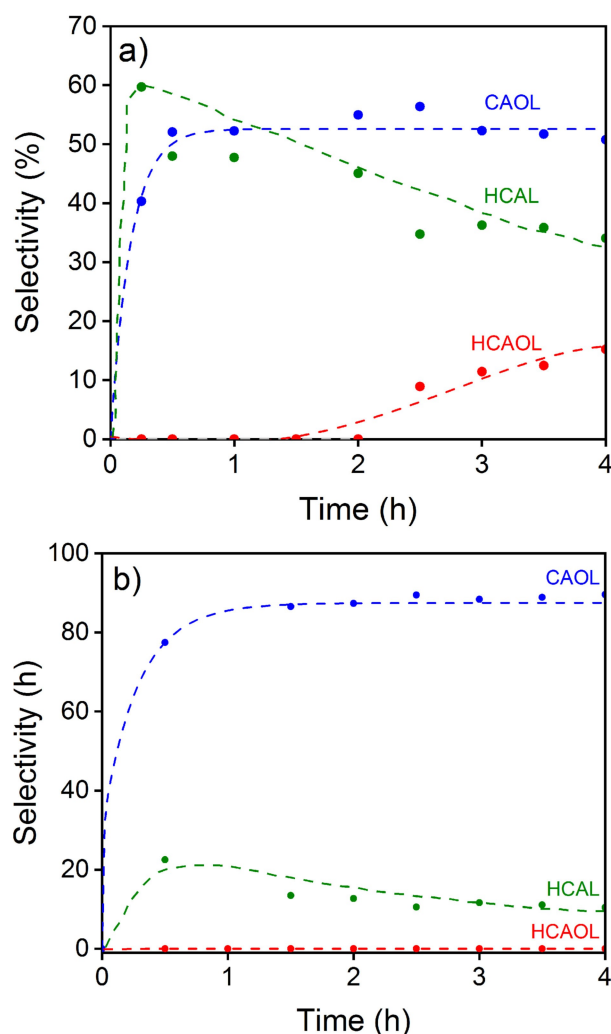

Figure 6. Selectivities in the hydrogenation of cinnamaldehyde (CAL) for a) NPs **1** and b) NPs **3** in [OMA][NTf$_2$] (reaction conditions: 80 °C, 10 bar H$_2$, Pt/Sn nanoparticles@IL/THF, 17 mmol CAL in 30 mL THF).

Conclusions

In summary, we report on a one-pot synthesis of bimetallic Pt/Sn and phase pure PtSn nanoparticles *via* the chemical reduction of the metal precursors, i.e. PtCl$_2$ and SnCl$_2$ or Sn(ac)$_2$ at 60 °C, followed by subsequent annealing at 200 °C. We investigated the influence of the nature of precursor, the molar precursor ratio and the type of IL on the crystallization process. The formation of SnO$_2$ formed as a side product was prevented by using SnCl$_2$ instead of Sn(ac)$_2$. The influence of the precursor ratio was studied for different molar ratios of PtCl$_2$/SnCl$_2$ (i.e. Pt:Sn 3:1, 3:2 and 3:3.) However, independent of the precursor ratio, the reduction of PtCl$_2$ and SnCl$_2$ in [OMA][NTf$_2$] never resulted in a single-phase product. In order to improve phase purity, the influence of the cation and anion of the IL was further investigated. It turned out, that reduction of PtCl$_2$ and SnCl$_2$ (Pt:Sn 3:1) with [BMIm][BEt$_3$H] in [BMIm][BF$_4$] resulted in the formation of phase pure and highly ordered, intermetallic PtSn NPs. In [BMIm][BF$_4$] microwave irradiation could be employed instead of conventional heating, resulting in highly crystalline PtSn NPs. The formation of initial, pre-reduction complexes of PtCl$_2$ and SnCl$_2$ in ILs was revealed by UV-vis spectroscopy. In contrast to the individual precursor solutions, UV-vis spectra of PtCl$_2$/SnCl$_2$ mixtures in [OMA][NTf$_2$] showed absorption peaks with maxima depending on the molar Pt:Sn precursor ratio. The solution of both precursors in [BMIm][BF$_4$] indicated the formation of a binary Pt–Sn complex with a maximum which was clearly shifted with respect to the respective solutions in [OMA][NTf$_2$]. Indeed, the nature of the complexes formed by the precursors in ILs seem to strongly influence the ordering behavior in the final intermetallic NPs. Eventually, catalytic performance was investigated employing the selective hydrogenation of cinnamaldehyde as a test reaction. Phase pure PtSn nanoparticles stabilized in [BMIm][BF$_4$] were catalytically inactive, most probably due to blocking of the NP surface by fluoride species derived from the $[BF_4]^-$ anion. While the reaction catalyzed by the monometallic Pt reference NPs yielded the saturated aldehyde (HCAL) as the only reaction product, a significantly higher selectivity to the α,β-unsaturated cinnamic alcohol was observed for the Pt/Sn-based NPs in [OMA][NTf$_2$]. Although NPs **1** (Pt/Pt$_3$Sn/SnO$_2$) revealed higher conversion of cinnamaldehyde (CAL), formation of fully hydrogenated product (HCAOL) was prevented in case of NPs **3** (Pt$_3$Sn/PtSn). Overall, our results clearly demonstrate the influence of the type of the IL on the ordering behavior and the phase composition of the NPs which in turn influence their catalytic performance. This opens up various possibilities for the future use of ILs for the synthesis of intermetallic NPs.

Experimental Section

All steps of NP synthesis and catalytic testing were carried out in anhydrous solvents under argon atmosphere. For synthesis of the reducing agents (i.e., methyltrioctylammonium triethyl-hydridoborate [OMA][BEt$_3$H], 1-butyl-3-methylimidazolium tri-ethylhydridoborate [BMIm][BEt$_3$H]) (see Supporting Information).

NP synthesis. Bimetallic Pt/Sn-based NPs were prepared from $PtCl_2$ and $Sn(ac)_2$ (NPs **1**: molar $PtCl_2/Sn(ac)_2$ ratio 3:1) or $SnCl_2$ (NPs **2**, NPs **6**, NPs **7**, NPs **8a**, and NPs **8b**: molar $PtCl_2/SnCl_2$ ratio 3:1; NPs **3**: molar $PtCl_2/SnCl_2$ ratio 3:2; NPs **4**: molar $PtCl_2/SnCl_2$ ratio 1:1). A total of 0.25 mmol metal salt precursor was dissolved in 4 mL IL (i.e., ([OMA][NTf$_2$]: NPs **1**, NPs **2**, NPs **3**, and NPs **4**), ([BMIm][NTf$_2$]: NPs **7**), ([BMIm][BF$_4$]: NPs **8a** and NPs **8b**), or ([BMIm][PF$_6$]: NPs **6**)) by evacuating for 2–3 h and stirring overnight. [OMA][BEt$_3$H] (3 mL, 1.5 M in THF) was added at 60 °C under stirring. The reaction mixture was then heated at 200 °C for 2–3 h to yield the dark brown to black NP dispersion in the IL. After cooling to room temperature, THF and BEt$_3$ were removed in vacuum. For synthesis of NPs **8b**, a Discover BenchMate^{TM} plus laboratory microwave by CEM was employed to heat the reaction mixture. For this purpose, the reaction mixture was loaded in a 25 mL, round-bottom Schlenk flask equipped with a magnetic stirrer and heated by microwave irradiation under argon in the *open vessel mode* (settings: 1) 60 °C, 10 W for 30 min; 2) 10 W, 200 °C for 1 h). An infrared sensor was employed for temperature monitoring. The reducing agent was added at 60 °C (30 min) and then further heated to 200 °C (1 h).

NP characterization. Particle size, morphology, and composition were analyzed by transmission electron microscopy (TEM, HAADF-STEM) using an aberration (image) corrected FEI Titan 80–300 (operated at 300 kV) equipped with an EDAX s-UTW EDX detector or a FEI Tecnai F20 (operated at 200 kV). For TEM analysis, the NP-IL sol was diluted by THF or the nanoparticles were precipitated and redispersed in dry THF. A small droplet of the sample was deposited on an amorphous carbon-coated, 400 mesh Cu grid in the anoxic glove box and transferred to the TEM using a Gatan 648 vacuum transfer holder. XRD studies were performed on a PANalytical X'Pert Pro X-ray diffractometer employing a Bragg-Brentano geometry with Cu Kα radiation and a Ni filter. The reflections were compared to reference data reported in the Joint Committee of Powder Diffraction Standards (JCPDS) data base: Pt (JCPD 03-065-2868), Pt$_3$Sn (JCPD 03-065-0958), and PtSn (JCPD 03-065-0959), SnO$_2$ (JCPD 00-046-1088). The NPs were deposited onto the sample holder and covered with Kapton foil in the anoxic glove box. Rietveld analysis (X'Pert Highscore Plus, PANalytical) was used to determine the phase composition of the NPs. The elemental composition of the particles was analyzed by OES-ICP (Agilent 725 ICP-OES Spectrometer, Agilent Technologies). UV-vis spectra were recorded with a Specord S600 UV-vis spectrometer (Analytic Jena) (see SI). The samples were loaded into the cuvette in the anoxic glovebox and closed with a Teflon stopper. The respective ILs were employed as a reference.

Catalytic tests. Hydrogenation reactions were carried out in an autoclave reactor (200 mL, Premex) which was equipped with a Teflon liner, a mechanical blowing stirrer (Teflon) and baffles (stainless steel), a thermocouple and a heating bath. In the anoxic glove box, 1–3 mL of the NPs@IL samples and the organic substrate (17 mmol CAL dissolved in 30 mL THF) were loaded in the autoclave reactor. After reaching the reaction temperature, stirring was started (1200 rpm). The reaction was started by hydrogen initiation into the reactor. During catalytic experiments, the hydrogen pressure was kept constant at 10 bar, and hydrogen was continuously supplied to the reactor by a gas burette (500 mL, Parr). The consumption of hydrogen was recorded automatically based on the pressure drop in the gas burette. The reaction products were analyzed by using a gas chromatograph (GC-FID, Agilent) equipped with a J&W SCIENTIFIC DB5 column (Agilent Technology, 30 m × 0.25 mm, 0.25 μm film thickness). The results were used to determine conversion and selectivity.

Product selectivity (S) and CAOL yield (Y_{CAOL}) were calculated using the following equations:

$$S_{CAOL} = \frac{[CAOL]}{[CAOL] + [HCAOL] + [HCAL]} 10^2$$

$$Yield_{CAOL} = S_{CAOL} \, X_{CAL} \, 10^{-2}$$

where [CAOL], [HCAOL] and [HCAL] is the concentration of CAOL, HCAOL and HCAL, respectively, at time t [mmol/L] and $X_{t,CAL}$ the conversion of cinnamaldehyde (CAL) after 3 h (%).

Acknowledgements

Conflict of Interest

The authors declare no conflict of interest.

[1] a) A. Llevot, B. Monney, A. Sehlinger, S. Behrens, M. A. R. Meier, *Chem. Commun.* **2017**, *53*, 5175–5178; b) S. Behrens, A. Heyman, R. Maul, S. Essig, S. Steigerwald, A. Quintilla, W. Wenzel, J. Bürck, O. Dgany, O. Shoseyov, *Adv. Mater.* **2009**, *21*, 3515–3519; c) D. I. Sharapa, D. E. Doronkin, F. Studt, J.-D. Grunwaldt, S. Behrens, *Adv. Mater.* **2019**, *31*, 1807381.

[2] a) S. Furukawa, T. Komatsu, *ACS Catal.* **2017**, *7*, 735–765; b) Y. Yan, J. S. Du, K. D. Gilroy, D. Yang, Y. Xia, H. Zhang, *Adv. Mater.* **2017**, *29*, 1605997-n/a; c) C. Dietrich, D. Schild, W. Wang, C. Kübel, S. Behrens, *Z. Anorg. Allg. Chem.* **2017**, *643*, 120–129; d) A. Egeberg, C. Dietrich, C. Kind, R. Popescu, D. Gerthsen, S. Behrens, C. Feldmann, *ChemCatChem* **2017**, *9*, 3534–3543; e) S. Furukawa, A. Yokoyama, T. Komatsu, *ACS Catal.* **2014**, *4*, 3581–3585; f) S. Furukawa, Y. Yoshida, T. Komatsu, *ACS Catal.* **2014**, *4*, 1441–1450; g) S. Wang, R. J. Lewis, D. E. Doronkin, D. J. Morgan, J.-D. Grunwaldt, G. J. Hutchings, S. Behrens, *Catal. Sci. Technol.* **2020**, *10*, 1925–1932; h) S. Furukawa, T. Komatsu, *ACS Catal.* **2016**, *6*, 2121–2125; i) A. K. Singh, Q. Xu, *ChemCatChem* **2013**, *5*, 652–676; j) S. Wang, R. J. Lewis, D. E. Doronkin, D. J. Morgan, J.-D. Grunwaldt, G. J. Hutchings, S. Behrens, *Catal. Sci. Technol.* **2020**, 10, 1925–1932.

[3] a) A. E. Alvarez, A. N. Gravina, J. M. Sieben, P. V. Messina, M. M. E. Duarte, *Mater. Sci. Eng. B* **2016**, *211*, 26–32; b) J. Yu, M. Jia, T. Dai, F. Qin, Y. Zhao, *J. Solid State Electrochem.* **2017**, *21*, 967–974; c) Y. Feng, C. Wang, D. Bin, C. Zhai, F. Ren, P. Yang, Y. Du, *ChemPlusChem* **2016**, *81*, 93–99.

[4] S. N. Coman, V. I. Parvulescu, M. De Bruyn, D. E. De Vos, P. A. Jacobs, *J. Catal.* **2002**, *206*, 218–229.

[5] a) G. Xu, J. Zhang, S. Wang, Y. Zhao, X. Ma, *RSC Adv.* **2016**, *6*, 51005–51013; b) P. D. Zgolicz, V. I. Rodríguez, I. M. J. Vilella, S. R. de Miguel, O. A. Scelza, *Appl. Catal. A* **2011**, *392*, 208–217; c) R. V. Maligal-Ganesh, C. Xiao, T. W. Goh, L.-L. Wang, J. Gustafson, Y. Pei, Z. Qi, D. D. Johnson, S. Zhang, W. Huang, *ACS Catal.* **2016**, *6*, 1754–1763.

[6] G. Ohloff, *Angew. Chem.* **1986**, *98*, 576–576; *Angew. Chem. Int. Ed.* **1986**, *25*, 582–582.

[7] G. Gmeiner, M. Seibicke, S. Behrens, B. Spliethoff, O. Trapp, *ChemSuSChem* **2016**, *9*, 583–587.

[8] a) A. J. Plomp, D. M. P. van Asten, A. M. J. van der Eerden, P. Mäki-Arvela, D. Y. Murzin, K. P. de Jong, J. H. Bitter, *J. Catal.* **2009**, *263*, 146–154; b) P. Gallezot, D. Richard, *Catal. Rev.* **1998**, *40*, 81–126.

[9]   a) X. Wang, J. Stöver, V. Zielasek, L. Altmann, K. Thiel, K. Al-Shamery, M. Bäumer, H. Borchert, J. Parisi, J. Kolny-Olesiak, *Langmuir* **2011**, *27*, 11052–11061; b) X. Wang, L. Altmann, J. Stöver, V. Zielasek, M. Bäumer, K. Al-Shamery, H. Borchert, J. Parisi, J. Kolny-Olesiak, *Chem. Mater.* **2013**, *25*, 1400–1407; c) D. Y. DeSario, F. J. DiSalvo, *Chem. Mater.* **2014**, *26*, 2750–2757.

[10] a) M. C. Román-Martínez, J. A. Maciá-Agulló, I. M. J. Vilella, D. Cazorla-Amorós, H. Yamashita, *J. Phys. Chem. C* **2007**, *111*, 4710–4716; b) A. D. Ballarini, P. Zgolicz, I. M. J. Vilella, S. R. de Miguel, A. A. Castro, O. A. Scelza, *Appl. Catal. A* **2010**, *381*, 83–91; c) C. T. Hable, M. S. Wrighton, *Langmuir* **1993**, *9*, 3284–3290; d) J. H. Kim, S. M. Choi, S. H. Nam, M. H. Seo, S. H. Choi, W. B. Kim, *Appl. Catal. B* **2008**, *82*, 89–102; e) I. Contreras-Andrade, A. Vázquez-Zavala, T. Viveros, *Energy Fuels* **2009**, *23*, 3835–3841; f) Q. Yi, J. Zhang, A. Chen, X. Liu, G. Xu, Z. Zhou, *J. Appl. Electrochem.* **2008**, *38*, 695–701; g) H. Rong, Z. Niu, Y. Zhao, H. Cheng, Z. Li, L. Ma, J. Li, S. Wei, Y. Li, *Chem. Eur. J.* **2015**, *21*, 12034–12041.

[11] L. Liu, A. Corma, *Chem. Rev.* **2018**, *118*, 4981–5079.

[12] a) E. W. Zhao, R. Maligal-Ganesh, C. Xiao, T.-W. Goh, Z. Qi, Y. Pei, H. E. Hagelin-Weaver, W. Huang, C. R. Bowers, *Angew. Chem. Int. Ed.* **2017**, *56*, 3925–3929; *Angew. Chem.* **2017**, *129*, 3983–3987; b) M. Chen, Y. Han, T. W. Goh, R. Sun, R. V. Maligal-Ganesh, Y. Pei, C.-K. Tsung, J. W. Evans, W. Huang, *Nanoscale* **2019**, *11*, 5336–5345.

[13] C. Vollmer, C. Janiak, *Coord. Chem. Rev.* **2011**, *255*, 2039–2057.

[14] a) S. Behrens, S. Essig, *J. Mater. Chem.* **2012**, *22*, 3811–3816; b) J. Dupont, J. D. Scholten, *Chem. Soc. Rev.* **2010**, *39*, 1780–1804.

[15] a) J. D. Scholten, B. C. Leal, J. Dupont, *ACS Catal.* **2012**, *2*, 184–200; b) E. Redel, J. Krämer, R. Thomann, C. Janiak, *J. Organomet. Chem.* **2009**, *694*, 1069–1075.

[16] a) R. Venkatesan, M. H. G. Prechtl, J. D. Scholten, R. P. Pezzi, G. Machado, J. Dupont, *J. Mater. Chem.* **2011**, *21*, 3030–3036; b) H. Konnerth, M. H. G. Prechtl, *Chem. Commun.* **2016**; c) T. N. Gieshoff, A. Welther, M. T. Kessler, M. H. G. Prechtl, A. Jacobi von Wangelin, *Chem. Commun.* **2014**, *50*, 2261–2264.

[17] a) K. Schutte, H. Meyer, C. Gemel, J. Barthel, R. A. Fischer, C. Janiak, *Nanoscale* **2014**, *6*, 3116–3126; b) K. Schutte, A. Doddi, C. Kroll, H. Meyer, C. Wiktor, C. Gemel, G. van Tendeloo, R. A. Fischer, C. Janiak, *Nanoscale* **2014**, *6*, 5532–5544; c) L. Schmolke, B. J. Gregori, B. Giesen, A. Schmitz, J. Barthel, L. Staiger, R. A. Fischer, A. Jacobi von Wangelin, C. Janiak, *New J. Chem.* **2019**, *43*, 16583–16594; d) A. Schmitz, H. Meyer, M. Meischein, A. Garzón Manjón, L. Schmolke, B. Giesen, C. Schlüsener, P. Simon, Y. Grin, R. A. Fischer, C. Scheu, A. Ludwig, C. Janiak, *RSC Adv.* **2020**, *10*, 12891–12899; e) L. Offner-Marko, A. Bordet, G. Moos, S. Tricard, S. Rengshausen, B. Chaudret, K. L. Luska, W. Leitner, *Angew. Chem. Int. Ed.* **2018**, *57*, 12721–12726; f) S. Wegner, M. Saito, J. Barthel, C. Janiak, *J. Organomet. Chem.* **2016**, *821*, 192–196; g) P. Arquillière, I. Helgadottir, C. Santini, P.-H. Haumesser, M. Aouine, L. Massin, J.-L. Rousset, *Top. Catal.* **2013**, 1–7.

[18] S. Essig, S. Behrens, *Chem. Ing. Tech.* **2015**, *87*, 1741–1747.

[19] C. W. Scheeren, G. Machado, J. Dupont, P. F. P. Fichtner, S. R. Texeira, *Inorg. Chem.* **2003**, *42*, 4738–4742.

[20] H. Bönnemann, W. Brijoux, R. Brinkmann, E. Dinjus, T. Joußen, B. Korall, *Angew. Chem. Int. Ed. Engl.* **1991**, *30*, 1312–1314.

[21] W. Chen, Z. Lei, T. Zeng, L. Wang, N. Cheng, Y. Tan, S. Mu, *Nanoscale* **2019**, *11*, 19895–19902.

[22] A. Weibel, R. Bouchet, F. Boulc, P. Knauth, *Chem. Mater.* **2005**, *17*, 2378–2385.

[23] L. Schmolke, S. Lerch, M. Bülow, M. Siebels, A. Schmitz, J. Thomas, G. Dehm, C. Held, T. Strassner, C. Janiak, *Nanoscale* **2019**, *11*, 4073–4082.

[24] C. Weidenthaler, *Nanoscale* **2011**, *3*, 792–810.

[25] J. F. Young, R. D. Gillard, G. Wilkinson, *J. Chem. Soc.* **1964**, 5176–5189.

[26] D. O. Downing, Z. Liu, B. W. Eichhorn, *Polyhedron* **2016**, *103*, 66–70.

[27] J. H. Nelson, W. L. Wilson, L. W. Cary, N. W. Alcock, H. J. Clase, G. S. Jas, L. Ramsey-Tassin, J. W. Kenney, *Inorg. Chem.* **1996**, *35*, 883–892.

[28] K. Schütte, J. Barthel, M. Endres, M. Siebels, B. M. Smarsly, J. Yue, C. Janiak, *ChemistryOpen* **2017**, *6*, 137–148.